Engineering of Molybdenum Sulfide Nanobunches on MWCNTs

Ali, Aya; Basuni, Mustafa; Shams-Eldin, Reham; Pilz, Lena; Hashem, Tawheed; Heinle, Marita; Nefedov, Alexei; Amin, Muhamed; Tsotsalas, Manuel; Drazic, Goran

Published in:
ACS Applied Nano Materials

DOI:
10.1021/acsanm.2c05311

Publication date:
2023

ACS APPLIED NANO MATERIALS

www.acsanm.org Article

Engineering of Molybdenum Sulfide Nanobunches on MWCNTs: Modulation of Active Sites and Electronic Conductivity via Controllable Solvothermal Deposition

Aya Ali,[#] Mustafa Basuni,[#] Reham Shams-Eldin, Lena Pilz, Tawheed Hashem, Marita Heinle, Alexei Nefedov, Muhamed Amin, Manuel Tsotsalas, Goran Drazic, Abdou Hassanien,* and Mohamed H. Alkordi*

Cite This: *ACS Appl. Nano Mater.* 2023, 6, 3627−3636 Read Online

ACCESS | Metrics & More | Article Recommendations | Supporting Information

ABSTRACT: Amorphous, mixed-valency, molybdenum sulfide (MoS_x) with a proposed formula, $[Mo^{(IV)}_4Mo^{(V)}_2(S_2^{2-})_3(S^{2-})_5](SO_4)_5$, was grown through a one-pot, solvothermal synthesis on multi-walled carbon nanotubes (MWCNTs) in a gram-scale setup. Optimizing the loading of the active catalyst relative to the conductive support resulted in optimized catalytic performance in hydrogen evolution reaction, reaching down to one of the lowest reported overpotentials, η_{10} = 140 mV and η_{100} = 198 mV with a Tafel slope of 62 mV/dec, for the 6.5 wt % of MoS_x@MWCNTs. Engineering this amorphous MoS_x catalyst was made possible through control of the oxidation state of Mo to avoid the fully reduced MoS_2 phases. We also demonstrate that engineering defects in the MoS_x catalyst does not require sophisticated techniques (e.g., UHV deposition, ion beam sputtering, and pulsed laser ablation) but can rather be induced simply through controlling the reductive synthesis conditions.

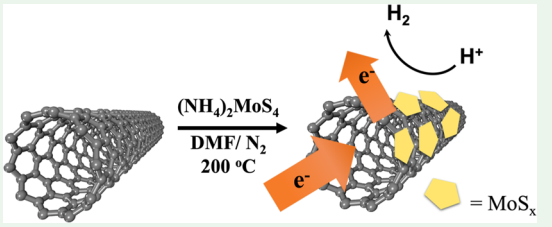

KEYWORDS: *amorphous MoS_x, molybdenum sulfide deposition on MWCNTs, molybdenum sulfide HER, supported nanocatalyst, mixed-valency molybdenum catalyst*

INTRODUCTION

The development of efficient and commercially viable catalysts for the hydrogen evolution reaction (HER),[1] and the focus on non-precious group compounds and carbon-supported catalyst,[2−4] especially MoS_2 in an acidic aqueous solution toward the HER,[5−8] spurred the interest of scientists to probe deeper the nature of the active sites and to improve the efficiency of this transition metal dichalcogenide. Detailed structure−activity investigations revealed that the edges of MoS_2 sheets are the active sites for the HER, with some contributions from basal defect sites and grain boundary sites.[9,10] Crystalline MoS_2 has three distinct phases, namely, tetragonal (1T), hexagonal (2H), and rhombohedral (3R),[11] where the digit denotes the number of MoS_2 layers per unit cell. As the catalytic activity of MoS_2 is ascribed to its edges and sulfur vacancies rather than its basal plane,[9,10] attempts to maximize the relative densities of such active sites have been extensively investigated. Examples of such previous attempts included doping with several transition metals into amorphous MoS_2 to promote its activity,[12] controllable disorder engineering, and oxygen incorporation in MoS_2 ultrathin nanosheets to simultaneously improve the electronic conductivity and abundance of active sites,[13] or through engineering the surface structure of MoS_2 to induce the formation of nanopores within the MoS_2 bicontinuous network to maximize the exposed edge sites.[14]

Attempts were also made to engineer S defects into the basal plane of MoS_2 as a possible way to improve the MoS_2 HER activity where gap states around the Fermi level allow hydrogen to bind directly to exposed Mo atoms.[15−19] However, dangling bonds in such defect sites might render the MoS_2 surface unstable under prolonged operation. More importantly, engineering such defects requires an elaborate setup and produces limited amounts of the catalyst that significantly hinders its wide-scale utilization. Previous reports demonstrated the feasibility of constructing composite structures of MoS_2 sheets and multi-walled carbon nanotubes (MWCNTs), producing wrapped nanotubes by partially bended stacks or hexagonal cylinders of MoS_2 layers,[20] or orthogonal attachment of MoS_2 sheets to the nanotube support.[21−23] Alternative to crystalline MoS_2 catalysts, amorphous MoS_x demonstrated high catalytic activity in promoting the HER, yet it is challenging to engineer such amorphous phases with desirable impact on activity.[24−26]

Received: December 15, 2022
Accepted: February 6, 2023
Published: February 16, 2023

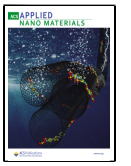

As electrocatalysts, the electronic conductivity of MoS_2 sheets is of major significance to their catalytic activity. The MoS_2 sheets are held together through van der Waals interactions, resulting in a significantly lower inter-plane electronic conductivity, with almost 2200 times higher resistivity as compared to an intraplanar (through the basal plane) conductivity of 0.1−1 $\Omega \cdot cm^{-1}$.[27,28] This intrinsic property of MoS_2 sheets endowed single-layer platelets deposited on a conductive support an optimal structure for high-efficiency MoS_2 catalysts, attainable through challenging fabrication techniques resulting in low catalyst loading on the support.

The approach outlined herein, Scheme 1, describes a pathway to controllably produce amorphous, mixed-valence,

Scheme 1. Deposition of Amorphous Mixed-Valence MoS_x Clusters on MWCNTs Providing Accessible HER Sites and Facilitated Electron Transport Pathway through the Conductive MWCNTs

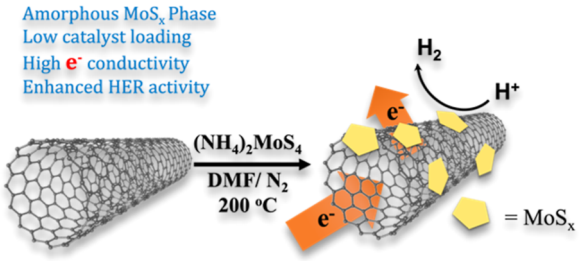

MoS_x nanoclusters deposited on MWCNTs, evading the formation of a lamellar MoS_2 structure. The deposited nanocluster catalyst structure, vide infra, allows for maintaining high abundance of catalytically active sites due to the cluster nature of the catalyst while simultaneously providing a facile pathway for electron transfer through the conductive support. We outline herein the significance of carefully selecting the reaction conditions leading to the formation of amorphous, mixed-valency MoS_x clusters with optimization of the MoS_x loading on the MWCNTs, and the underlying implications on its catalytic activity. This engineered catalyst provides for addressing several challenges, namely, (i) enhancing the density of active sites, (ii) ensuring enhanced electronic conductivity by the support, (iii) controlling the wt % of the active catalyst, and (iv) the ability to generate gram scale of the catalyst in a facile one-pot solvothermal synthesis.

EXPERIMENTAL SECTION

Instrumentation and Measurements. All reagents were of commercial grade used without further purification. Electrochemical measurements were conducted in a three-electrode system using Ag/AgCl as the reference electrode (Hanna Instruments, HI 5314, 3.5 M KCl), glassy carbon as the working electrode, and a graphite rod as the counter electrode. Measurements were recorded on a Bio-Logic potentiostat/galvanostat SP-50, and data were recorded using EC-lab software. Electrochemical impedance spectroscopy (EIS) was performed on a PalmSens potentiostat, and data was recorded with a PS-traces 5.8. EIS measurements were carried out in 0.5 M H_2SO_4, with a glassy carbon electrode (GCE) as the working electrode, a graphite rod as the counter electrode, and Ag/AgCl as the reference electrode, at voltage amplitudes of 10 mV and frequencies ranging from 0.1 to 10^5 Hz. X-ray photoelectron spectroscopy (XPS) measurements were carried out under an ultra-high vacuum with a base pressure of 1×10^{-9} mbar. Core-level spectra were recorded under normal emission with a Scienta R4000 analyzer using Al Kα radiation. EIS was performed on a PalmSens4 potentiostat, and data was recorded with a PS-traces 5.8. Fourier transform infrared spectra were recorded on a ThermoScientific iS10 spectrophotometer. Thermogravimetric analyses were performed on a TA Q-50 instrument operated under nitrogen flow. Contact angle measurements were performed on a Biolin ThetaLite optical tensiometer.

Reagents and Synthesis. Carboxylated MWCNTs (MWCNT-COOH) > 95 wt %/30−50 nm were purchased from Cheap Tubes (SKU: 050306). Ammonium tetrathiomolybdate, 99.95% (metal basis), was purchased from Alfa Aesar. 2-Propanol, *N*,*N*′-dimethylformamide (DMF) analytical reagent grade 99.99%, and ethanol (absolute high-performance liquid chromatography gradient grade) were purchased from Fisher Chemicals. In a pressure vessel, charged with a magnetic stir bar, 45 mL of DMF was degassed through three cycles of applying vacuum and flushing back with N_2, to which was then added 200 mg of MWCNTs-COOH and the increasing amounts of $(NH_4)_2MoS_4$ (26, 53, and 80 mg); then, the vessel was sealed with a Teflon screw cap under a N_2 atmosphere. The mixture was briefly sonicated and then placed in an oil bath at 200 °C with stirring for 24 h. The reaction mixture was then cooled to room temperature and filtered through a Nylon filtration membrane and washed with DMF, followed by washing with ethanol, and the collected black solid was dried at 100 °C for 1 h.

Elemental Analysis. Three samples each containing 10 mg of the material were weighed out with a Mettler AT261; to each sample was added 5 mL of aqua regia (HCl/HNO_3 Suprapur) and heated in a boiling water bath for 3 h; then the solution was made up to 10 mL volume with aqua regia. The digested samples were then diluted with H_2O type 1 and quantified with ICP-OES (Optima 8300DV, PerkinElmer) for Mo (202.031, 203.845, 204.597, and 281.616 nm) and S (181.975, 180.669, and 182.563 nm) using a calibration series up to 50 mg/L. The spike recovery was between 90 and 110%. All measurements were done in axial plasma viewing, and data is presented in Table S1.

General Procedure for Ink Preparation. For each sample, ∼8 mg of the active material was dispersed in 1 mL of ^{i}PrOH to which was added 40 μL of Nafion (5 wt % in ^{i}PrOH). The mixture was sonicated for 10 min before casting an aliquot of 20 μL on a polished GCE. The casted mixture was left to dry at room temperature, followed by another casting of 20 μL and drying prior to measurements in 0.5 M H_2SO_4.

Contact Angle Measurements. Contact angle measurements were performed by depositing 0.5 mL of the same ink suspension used for the electrochemical characterization on a glass slide (a casted area of 1 × 1 cm), followed by drying at 90 °C for 15 min before testing.

STM Measurements. In order to prepare a suitable sample for STM measurements, the powder sample of MoS_2@MWCNTs was sonicated in isopropanol for 30 sec to form a diluted dispersion before a few drops (∼10μl) being cast on atomically flat Au(111) substrate. The Au(111) substrate was prepared earlier by several cycles of sputtering and annealing to ensure atomically clean surface. The wet sample was left to dry spontaneously for 20 minutes before loading into the UHV chamber. The structure was characterized by a commercial ultra-high vacuum Joule Thomson (SPECS Surface Nano Analysis GmbH) STM. Measurements were carried out 4 K substrate temperature with tunneling current of 30 pA and with bias voltages of 3V range. High quality images were recorded in constant current mode. The images presented here have not been processed in anyway.

RESULTS AND DISCUSSION

Herein, the catalyst design utilized the excellent electronic conductivity of MWCNTs, upon which MoS_x clusters were deposited from thermal disproportionation of $(NH_4)_2MoS_4$. In this design, optimization of the MoS_x loading onto the carboxylate-functionalized MWCNTs was achieved by controlling the concentration of the soluble ammonium thiomolybdate, keeping the same mass of suspended MWCNTs constant. It was anticipated that the surface-

https://doi.org/10.1021/acsanm.2c05311
ACS Appl. Nano Mater. 2023, 6, 3627−3636

functionalized MWCNTs will induce seeding and subsequent growth of MoS_x clusters at the MWCNTs. Overall, the key elements in our design were (1) utilizing a highly electronically conductive support, (2) facile solvothermal synthesis to deposit MoS_x on such support, (3) controlling the reaction conditions to result in mixed-valence amorphous and highly dispersed MoS_x clusters, (4) optimizing the MoS_x/support ratio to arrive at optimal loading that balances the abundance of catalytic sites against their low electronic conductivity, and (5) the scalability of the synthesis method utilizing relatively inexpensive reagents and an uncomplicated synthesis technique. While previous reports examined compositing MoS_2 and MWCNTs,[22,29] engineering the deposition of the amorphous MoS_x phase on MWCNTs and optimizing the mass loading to balance the overall active site abundance and electronic conductivity are, to the best of our knowledge, first explored herein. The facile solvothermal synthesis utilized herein allowed for the synthesis of a relatively large amount of the solids through a one-pot technique, surpassing cumbersome procedures to deposit MoS_x on the conductive support. Moreover, by simply controlling the relative amounts of the precursors added to the initial mixture, variable MoS_x content could be deposited on the MWCNTs. As indicated by elemental analysis of acid-digested samples, three loadings of MoS_x on MWCNTs were attained (6.5, 10.2, and 17.3 wt %). MoS_x formed through the solvothermal reduction in DMF appeared to be amorphous, as indicated by the X-ray diffraction (XRD) patterns recorded for the three compounds with variable wt % of MoS_x in the composite, Figure 1. In

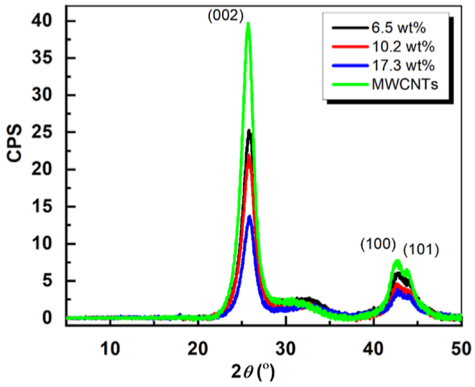

Figure 1. XRD patterns for the MoS_x@MWCNTs indicating their amorphous nature, different loadings of MoS_x wt % are indicated in the legend.

Figure 1, three diffraction peaks were observed at 2θ of 25.79, 42.79, and 43.9°, corresponding to the diffraction from the MWCNT (002), (100), and (101) planes, respectively. As no extra peaks were observed, this indicated the amorphous nature of the deposited catalyst. It is also noticed that the peak intensities for the samples collected under similar conditions showed decreased crystallinity, that is, increased amorphous content, upon increasing the MoS_x wt % in the composites. Amorphous MoS_x was previously shown to demonstrate excellent catalytic activity, sometimes surpassing crystalline phases due to higher abundance of active sites present in their structures.[24] However, compared to a previous study by Jaramillo et al. on amorphous MoS_x,[24] the benefit of formulating amorphous MoS_x on MWCNTs is obviated here, in terms of the overall catalyst performance, vide infra.

Scanning Electron Microscopy and Scanning Tunneling Microscopy Characterization. The scanning electron microscopy (SEM) image taken for the best performing catalyst (6.5 wt % of MoS_x@MWCNTs) is shown in Figure 2,

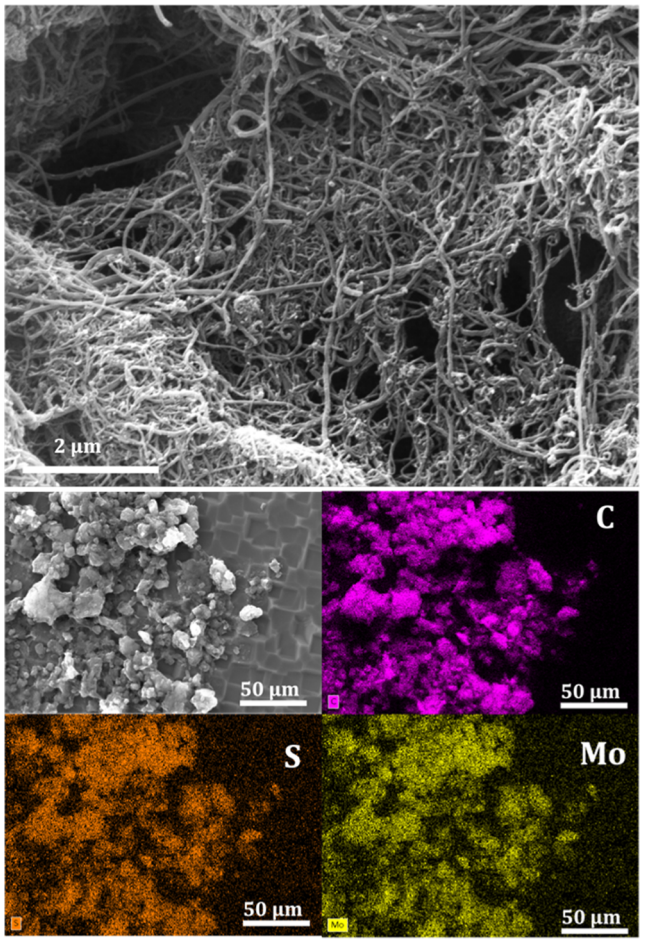

Figure 2. SEM image of the MoS_x@MWCNTs showing no evidence for the formation of agglomerates or particulates of MoS_x outside the MWCNT matrix and the EDX maps (imaged at lower magnification for clarity) showing excellent tracing of the elemental (C, S, and Mo) maps to that of the SEM image.

with no visible formation of MoS_x particulates or agglomerates outside the MWCNT matrix, indicating uniform deposition of MoS_x on the MWCNTs during the solvothermal synthesis. The energy-dispersive X-ray (EDX) mapping of MoS_x@MWCNTs in Figure 2 clearly demonstrates the homogeneity of the MoS_x deposition where the Mo and S elemental maps essentially traced those of C from the MWCNTs. The SEM images of the samples with higher MoS_x wt % (Figure S1 in the Supporting Information) showed the tubes with no extra agglomerates or particulates of MoS_x for the sample with 10.2 wt %; however, the sample containing 17.3 wt % of MoS_x showed a bicontinuous thin film of MoS_x bridging the MWCNTs. Scanning transmission electron microscopy with high-angle annular dark-field (HAADF) and bright-field (BF) imaging of the sample, Figure 3, clearly demonstrated deposition of the MoS_x nanoparticles onto the MWCNTs, with no notable crystallinity further confirming the finding of the XRD analysis. Further characterization of the catalyst was conducted through scanning tunneling microscopy (STM),

https://doi.org/10.1021/acsanm.2c05311
ACS Appl. Nano Mater. 2023, 6, 3627−3636

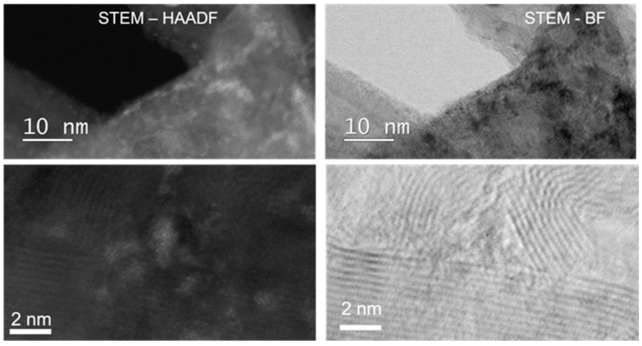

Figure 3. STEM-HAADF and BF images of the MoS_x@MWCNTs showing the nanoparticles of MoS_x coating the MWCNTs (bright spots in the HAADF and dark spots in the BF images).

Figure 4. In Figure 4a, nanoclusters of MoS_x are shown to be homogeneously coating the MWCNTs, while at a higher magnification in Figure 4b, the MoS_x clusters are shown to be tracing the surface of the MWCNTs and with no long-range order. This lack of long-range order further supports the findings of the XRD analysis, indicating the amorphous nature of the catalyst. Higher resolution STM imaging of the nanoclusters demonstrated bundles of stacked rod-like structures, Figure 4c, resembling a banana bunch, where each element of the cluster has a length of ∼1.8 nm and a diameter in the range of ∼0.38 nm. This observation indicates that the true catalyst is composed of short linear polymeric chains of MoS_x grouped through relatively strong interactions, potentially the electrostatic ones, with a relatively small number of such short-chain elements clustering together through weaker interactions into nanoclusters coating the surface of the MWCNTs. Although the images were recorded at cryogenic 4 K temperature for maximal resolution by damping thermal noise, atomistic resolution of the catalyst was not feasible due to the challenging nature of the sample, with a multitude of surface curvature and roughness, as compared to otherwise atomically resolved images attained on atomically flat surfaces. Nevertheless, the high-resolution images unravel the inner structure of individual rods where the MoS_x clusters form short chains of size ∼1.8 nm with a lattice spacing of 0.38 nm, Figure 4c. Although the clusters show some degree of intricate short-range order, the overall structure is rather complex and does not form any long-range order, indicating weakly bonded clusters. Indeed, at high tunneling current (>500 pA), individual clusters can be spontaneously picked up by the STM tip.

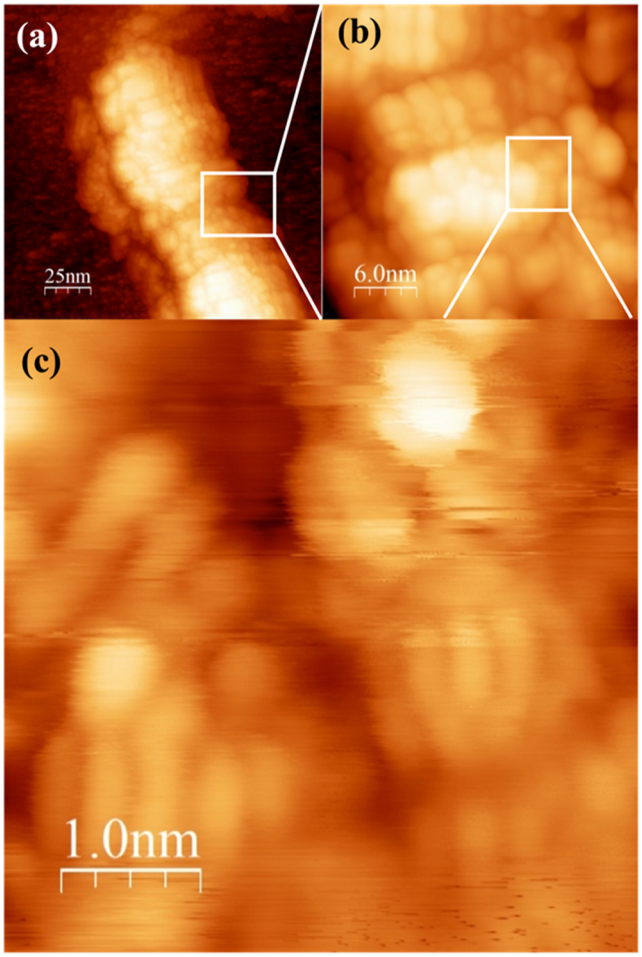

Figure 4. STM images of the MoS_x@MWCNTs showing (a) one MWCNT coated homogeneously with the MoS_x nanoclusters, (b) topography of the MoS_x clusters showing multi-layer stacks on the MWCNT, and (c) higher resolution image showing rod-like nanoclusters of MoS_x (∼1.8 nm × 0.38 nm) with no long-range periodicity. All images were recorded in the constant current mode at a temperature of 4 K. The tunneling parameters are 3 V and 30 pA for sample bias and tunneling current, respectively.

X-ray Photoelectron Spectroscopy. The XPS detailed spectra for the 6.5 wt % of MoS_x@MWCNTs (Mo 3d, S 2p, C 1s, and O 1s lines) are shown in Figure 5. The C 1s spectrum was successfully deconvoluted to a number of individual components for different carbon configurations: C═C (284.4 eV), C−C/C−H (285.3 eV), C−O (286.2 eV), C═O (288.4 eV), and a $\pi-\pi^*$ shake-up satellite (290.6 eV), in typical similarity to the spectra of MWCNTs.[30] The Mo 3d detailed spectrum was deconvoluted into two chemical environments, where Mo $3d_{5/2}$ lines were recorded at 229.14 and 232.78 eV, with a relative intensity ratio of 2:1, respectively. The two Mo doublets were fitted at a fixed splitting of 3.13 eV, keeping the intensity ratio of 3:2 between Mo $3d_{5/2}$ and Mo $3d_{3/2}$ lines. The observed shifts are in good agreement with Mo(IV) and Mo(V) oxidation states, respectively.[31] The Mo signals could potentially be assigned to Mo−O or Mo−S bonds,[32] where an appreciable oxygen content was recorded with higher relative oxygen atom % as compared to the pristine MWCNTs. The O 1s signal was fitted with two lines centered at 531.4 and 533.4 eV with a relative intensity of 10:1, respectively. The signal at 533.4 eV was also recorded for the partially oxidized MWCNT support, and thus, the signal at 531.4 eV can be assigned to S−O from SO_4^{2-} ions. The S 2p signal was fitted by three components, demonstrating S $2p_{3/2}$ lines at 161.73, 162.86, and 169.7 eV. The relative intensity ratio of the S $2p_{3/2}$ peaks was 1.2:1.4:1. The signal at 161.73 eV could be ascribed to bridging unsaturated S^{2-} (bridging two Mo ions) or terminal S_2^{2-} (coordinated to one Mo ion) ligands, while the signal at 162.86 eV could be ascribed to bridging S_2^{2-} (coordinated to two Mo ions) or apical S^{2-} ligands (coordinated to three Mo ions).[33,34] Finally, the signal at 169.7 eV could be ascribed to SO_4^{2-} ions, bridging the clusters through Mo−O bonds. The S 2s spectrum was deconvoluted into three components at binding energies of 225.7, 226.6, and 233.2 eV, further confirming the assignments made using the S 2p spectra for three distinct S chemical environments. While the signal at

https://doi.org/10.1021/acsanm.2c05311
ACS Appl. Nano Mater. 2023, 6, 3627−3636

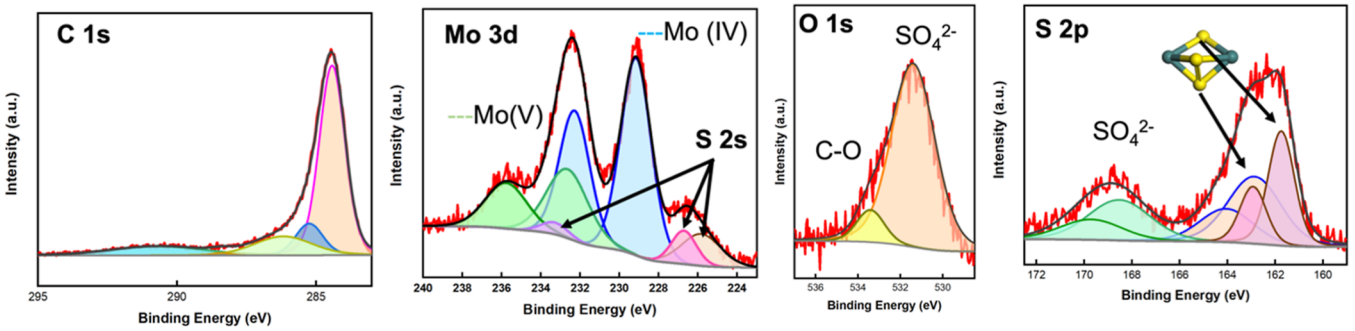

Figure 5. XPS spectra for the MoS_x@MWCNTs, (red) experimental data, (black) sum envelope, and doublet signals for Mo 3d and S 2p are indicated with the same color.

higher binding energy could be ascribed to the SO_4^{2-} ions, the latter two could be assigned to bridging (S_2^{2-}) and unsaturated (S^{2-}) species, respectively.[35] The relative peak areas divided by each element's relative sensitivity factor were used to derive a plausible composition of the catalyst's surface. A relative S 2p/Mo 3d adjusted peak area was 1.93, and the ratio of $(SO_4)^{2-}$ to Mo was ~5:6. A plausible empirical formula could then be proposed based on the observed relative intensities and speciation, as $[\mathbf{Mo^{(IV)}_4Mo^{(V)}_2(S_2^{2-})_3(S^{2-})_5](SO_4)_5$. In this proposed formula, three disulfide ions are presumed to be in the bridging (μ_2-S_2^{2-}) mode, and five sulfide ions assume the unsaturated (μ_2-S^{2-}) mode, as demonstrated previously for the different S species in MoS_2 or its clusters.[34,36,37] This arrangement apparently maximizes the relative abundance of the more catalytically active unsaturated S sites within a relatively small ~1.8 nm cluster size, with enhanced surface-to-volume ratio. Combining these two aspects of the catalyst, higher relative abundance of more active S sites and small cluster size with a larger surface-to-volume ratio appear to have considerably contributed to the overall enhanced activity reported herein.

Modeled Structure of the Catalyst. A good insight into the plausible active sites in the catalyst in hands can be drawn from previous studies conducted on molecular clusters with well-defined S sites. The dimeric $[Mo_2S_{12}]^{2-}$ cluster with only two types of S sites (bridging S_2^{2-} and terminal S_2^{2-}) showed higher catalytic activity toward the HER as compared to trimeric $[Mo_3S_{13}]^{2-}$ with additional types of apical S^{2-} sites, indicating lower activity of the apical S sites.[37] Indeed, theoretical studies indicated higher HER activity, demonstrating lower free energy of the system undergoing H adsorption on bridging S sites as compared to apical S sites, where the bridging sites demonstrated lower Gibbs free energy by 1 eV as compared to apical sites.[34] We constructed the structure shown in Figure 6 as a plausible model of the catalyst in hand. The proposed structure fulfills the stoichiometry determined from the XPS analysis for the Mo(IV), Mo(V), S^{2-}, and S_2^{2-} species, as well as the stoichiometry of the sulfate counterions with a plausible binding mode to the Mo backbone. The structure was terminated by monovalent (HSO_4^-) ions as potential sites for crosslinking neighboring chains. This proposed structure was subjected to DFT optimization at high spin using Gaussian09 and the B3LYP functional. The 6-31G basis sets are used for all atoms except the Mo, which is represented by the LANL2DZ basis sets with effective core potential. The solvent effect was included using the polarizable continuum model. The geometry-optimized short-chain oligomeric structure model shown in Figure 6 represents a

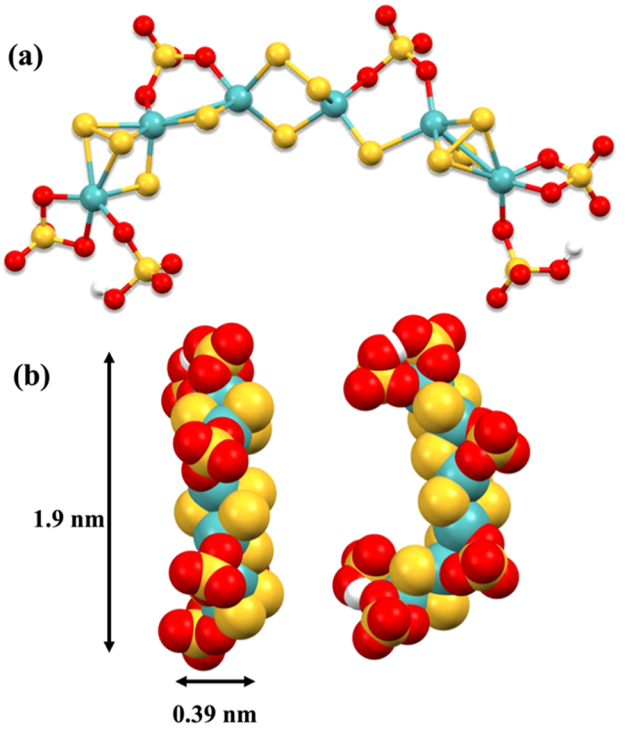

Figure 6. (a) Geometry-optimized model structure of the mixed-valence amorphous MoS_x, demonstrating bridging S ions (S^{2-} and S_2^{2-}) and Mo-coordinated sulfate counterions, and (b) space fill representation of the structure at different orientations showing the dimensions of the individual chain.

simple fragment satisfying the empirical formula, as determined from the surface analysis, where condensation into clusters of sulfate-bridged chains is expected due to the observed insolubility of the catalyst. Moreover, the proposed oligomeric structure is in good agreement with the observed surface structure probed by STM, where the modeled structure demonstrates a curved nanorod of ~1.9 nm length that can potentially undergo self-assembly through bridging sulfate ions into nanobunch clusters shown in Figure 4.

Electrochemical Catalytic Activity. The electrochemical catalytic activity of the three samples of MoS_x@MWCNTs was tested in an acidic solution as shown in Figure 7, including the MWCNTs as the control. The catalyst containing 6.5 wt % of MoS_x in the composite demonstrated the most enhanced catalytic activity toward the HER. It is also clear that a decreasing HER activity was noticed upon increasing the wt % of MoS_x in the composite. This is evident from the

https://doi.org/10.1021/acsanm.2c05311
ACS Appl. Nano Mater. 2023, 6, 3627−3636

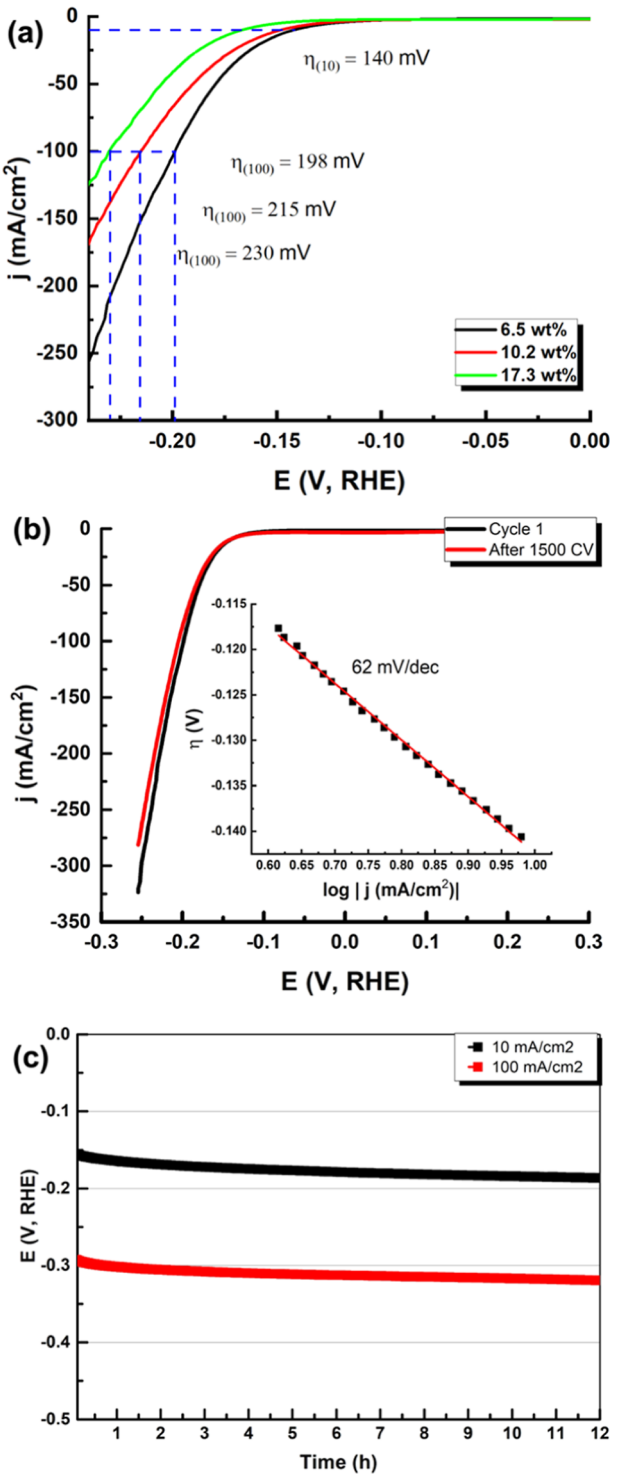

Figure 7. (a) LSV scans of the different MoS_2 loading on MWCNTs and that of MWCNTs, (b) LSV scans for the 6.5 wt % of MoS_2@MWCNTs showing its stability after extended cycles and in inset of the corresponding Tafel plot, and (c) CP plot for the 6.5 wt % of MoS_2@MWCNTs indicating its extended stability at two different current density values. All measurements were conducted in the 0.5 M H_2SO_4 solution.

overpotential needed to derive a current density of 10 mA/cm^2 (η_{10}) or 100 mA/cm^2 (η_{100}) utilizing the MoS_x@MWCNTs as the catalyst deposited on the working electrode, Figure 7a. The exceptionally low overpotential (η_{10} = 140 mV and η_{100} = 198 mV) for the 6.5 wt % of MoS_x as compared to the overpotentials recorded using higher MoS_x wt % is also notable. We also attempted the synthesis of lower wt % (3.5 wt %) of MoS_x@MWCNTs, where upon testing it resulted in η_{100} = 240 mV (Figure S2), confirming that the optimal loading is 6.5 wt % of MoS_x@MWCNTs. The steady increase in overpotentials that are needed to derive the same current densities upon increasing the MoS_x wt % indicated the existence of an optimal balance between MoS_x loading and performance of the overall catalyst. The linear sweep voltammetry (LSV) curves recorded at the beginning of the HER and those recorded after 1500 CV scans indicated the excellent stability of the composite, Figure 7b. The inset in Figure 7b shows the Tafel plot with a Tafel slope of 62 mV/dec, similar to that reported previously for amorphous MoS_x.[24] According to the previous literature,[13] for MoS_2 catalysts, Tafel slopes in the range of 40−60 mV dec^{-1} are taken to indicate a disordered catalyst structure with a relatively complex reaction mechanism in-between that of Volmer adsorption and Heyrovsky desorption steps as the rate-limiting step. Finally, as a measure of stability of the catalyst, chronopotentiometry (CP) measurements at two current densities (10 and 100 mA/cm^2), Figure 7c, were conducted, which indicated a maintained overpotential for 12 h of continuous electrolysis.

Moreover, the catalyst demonstrated higher HER activity as compared to other MoS_2 catalysts reported previously, Figure 8 and Table S2, Supporting Information. When compared to other reported MoS_2 catalysts, the MoS_x@MWCNTs demonstrated one of the smallest reported overpotentials to derive a catalytic current density of 10 mA/cm^2, demonstrating that the higher catalytic activity can be linked to reduced ohmic losses due to better contact with the current collector or enhanced reactant diffusion due to the porous structure. Notably, Hu and co-workers demonstrated that the activity of MoS_2 toward the HER can be enhanced when physically mixed with MWCNTs (the best performance was recorded for 200 wt % of MWCNTs).[38] However, we demonstrate here that the in

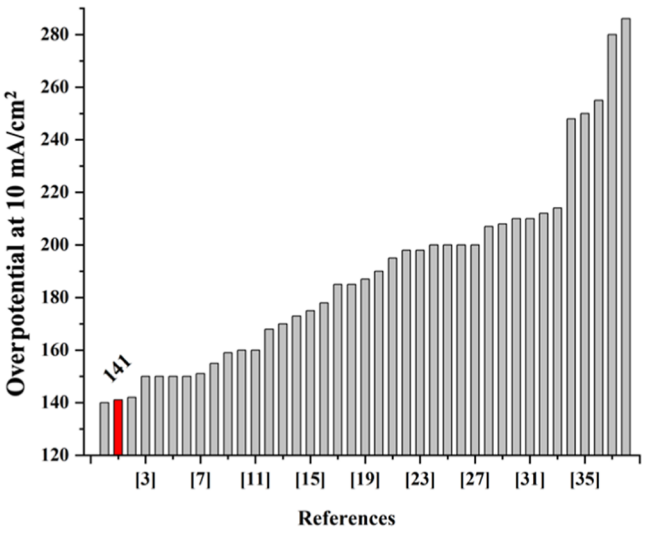

Figure 8. Plot of overpotentials reported to derive a current density of 10 mA/cm^2 from different MoS_2 HER catalysts, the result of the current study is highlighted, and references are reported in the Supporting Information.

https://doi.org/10.1021/acsanm.2c05311
ACS Appl. Nano Mater. 2023, 6, 3627−3636

situ growth of MoS_x on the MWCNTs produces a much better catalyst, vide infra.

Calculation of Turnover Frequency. The turnover frequency (TOF, s^{-1}), defined as the HER rate per active site per time, was calculated as

$$\mathrm{TOF}\ (s^{-1}) = \left| j\ (\mathrm{A\ cm^{-2}}) \times S\ (\mathrm{cm^2})\ \frac{1\mathrm{H_2}}{2e^{-1}} \times \frac{1e^{-1}}{q_e} \right| / N_{\mathrm{active}}$$

where j is the current density, obtained from the LSV during the HER, S is the geometric surface area of the working GCE (0.07 cm^2), and q_e is the elementary charge (1.602×10^{-19} C). N_{active} is the number of Mo atoms assumed to be the active sites. It was assumed that all the Mo atoms in the clusters were involved in the catalysis (lowest bound limit). N_{active} was obtained from ($N_{active} = m \times N_A$), where m is the molar number of MoS_x loaded on the electrode ($mol_{Mo} \cdot cm^{-2}$) and N_A is Avogadro's number (6.022×10^{23}). All percentages of Mo and S were obtained by the ICP-OES elemental analysis. Although direct measurements of TOF might be cumbersome especially if more than one active site is involved in the reaction, calculations of the overall TOF of the electrode material are highly relevant to assess the catalyst activity. The structure of the active sites, especially their ability to bind the active intermediates and the activation energies required to derive the catalytic processes, determines the macroscopic physical and chemical properties of the electrocatalyst's surface. In the absence of a direct method to measure the TOF for each type of active sites present at the electrocatalyst, calculations of the overall TOF, averaged over the total number of active sites, are a commonly accepted measure to compare one electrocatalyst performance to another.[29,39] We reported the TOF in units of H_2 s^{-1} per surface Mo atom to compare the catalyst performance to other molybdenum sulfide HER catalysts. This treatment avoids difficulties in distinguishing the activity among different sulfur sites. The TOFs for the 6.5, 10.2, and 17.3 wt % of MoS_x@MWCNT catalysts were 0.3, 0.12, and 0.05 H_2 s^{-1} per Mo atom, respectively, at η = 200 mV versus RHE, Figure 9. The calculated TOF of 0.3 H_2 s^{-1} for the catalyst containing 6.5 wt % of MoS_x compares favorably with that reported previously for thiomolybdate nanoclusters on the GCE at an overpotential of 200 mV, demonstrating a TOF of 0.15 H_2 s^{-1}, testifying to the excellent performance of the catalyst in hand.[40] To further probe the fundamental processes contributing to the overall observed performance of the catalysts, EIS was employed, Figure 10. The EIS data collected for the MWCNTs as well as the three catalysts prepared with increasing MoS_x content was fitted by a simple Randles' circuit. The two resistive components in this circuit are (i) the combined solution and electrode interface resistivity regarded as a simple resistive component and denoted as R_{int} and (ii) the charge-transfer resistivity (R_{CT}) which accounts for the impedance of the catalyst/support against the mobility of the charge carriers and hence thought to directly impact the kinetics of the catalyst. The third component in the circuit is the capacitive constant-phase element (CPE) which reflects the ability of the system to store energy through surface-adsorbed charges in a capacitive action. In fact, the data fitting indicated similar R_{int} for the different material due to the similarity of the testing solution and electrode configuration (8−10 Ω). However, a notable increase in R_{CT} was evident upon increasing the MoS_x relative composition, from 6.5 to 10.2 wt % and even goes to a much higher value at the composite with 17.3 wt % of MoS_x (312.4, 378.3, and 642 Ω, respectively). This observation clearly indicates the decreased charge mobility upon increasing the MoS_x content, which is expected given the reduced inter-particle electronic mobility within the MoS_x nanosheets stacked together by weak van der Waals forces, as compared to the basal plane electronic conductivity within each sheet. The highest R_{CT} recorded was for the MWCNTs, which could be ascribed to the lack of active catalytic centers for HER on their surface. The EIS fitting also allowed extracting the Q value, indicative of the capacitance of the electrode material with the unit $T = F\ s^{(\theta-1)}\ cm^{-2}$, where F is Farad, θ is the constant-phase exponent, and s is second. As the three samples were fitted with a similar constant-phase exponent and using the same electrode surface area, the decreased Q values for the CPE going from lowest MoS_x loading to the highest can be taken to represent decreased abundance of active proton adsorption sites upon increasing the MoS_x content in the composite. This observation can be ascribed to decreased relative abundance of S active sites upon increasing the stacking of the MoS_x nanocluster coat atop the MWCNTs. The Q value for the MWCNTs is considerably low, as compared to its composites with MoS_x. The much higher Q values for the MoS_x@MWCNTs as compared to the pristine MWCNTs can be attributed to the facilitated proton adsorption at the MoS_x edges, in turn constituting the major charge storage process as an electrochemical double-layer capacitor. Therefore, coupling of facilitated electron transfer (low R_{CT}) with enhanced proton adsorption sites (high Q) resulted in the optimal observed performance in the MoS_x@MWCNTs with 6.5 wt % of MoS_x, as compared to higher MoS_x loadings or the pristine MWCNTs.

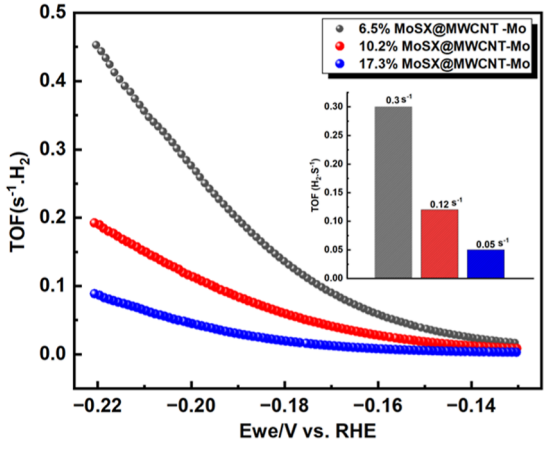

Figure 9. TOF for the three catalysts of MoS_x@MWCNTs with increasing MoS_x wt % at different applied bias values; the inset shows the TOF for the three catalysts at an overpotential of 200 mV vs RHE, values calculated based on Mo sites.

Surface Wettability Measurements. An additional potential factor to consider in the interpretation of the observed activity of the different material explored here is the surface wettability in the electrolyte. An increased hydrophobicity of the catalyst is expected to negatively impact its activity in the aqueous solution. Therefore, we opted to measure the contact angle for the MWCNTs and the three different catalysts prepared, Figure 11, using the same

https://doi.org/10.1021/acsanm.2c05311
ACS Appl. Nano Mater. 2023, 6, 3627−3636

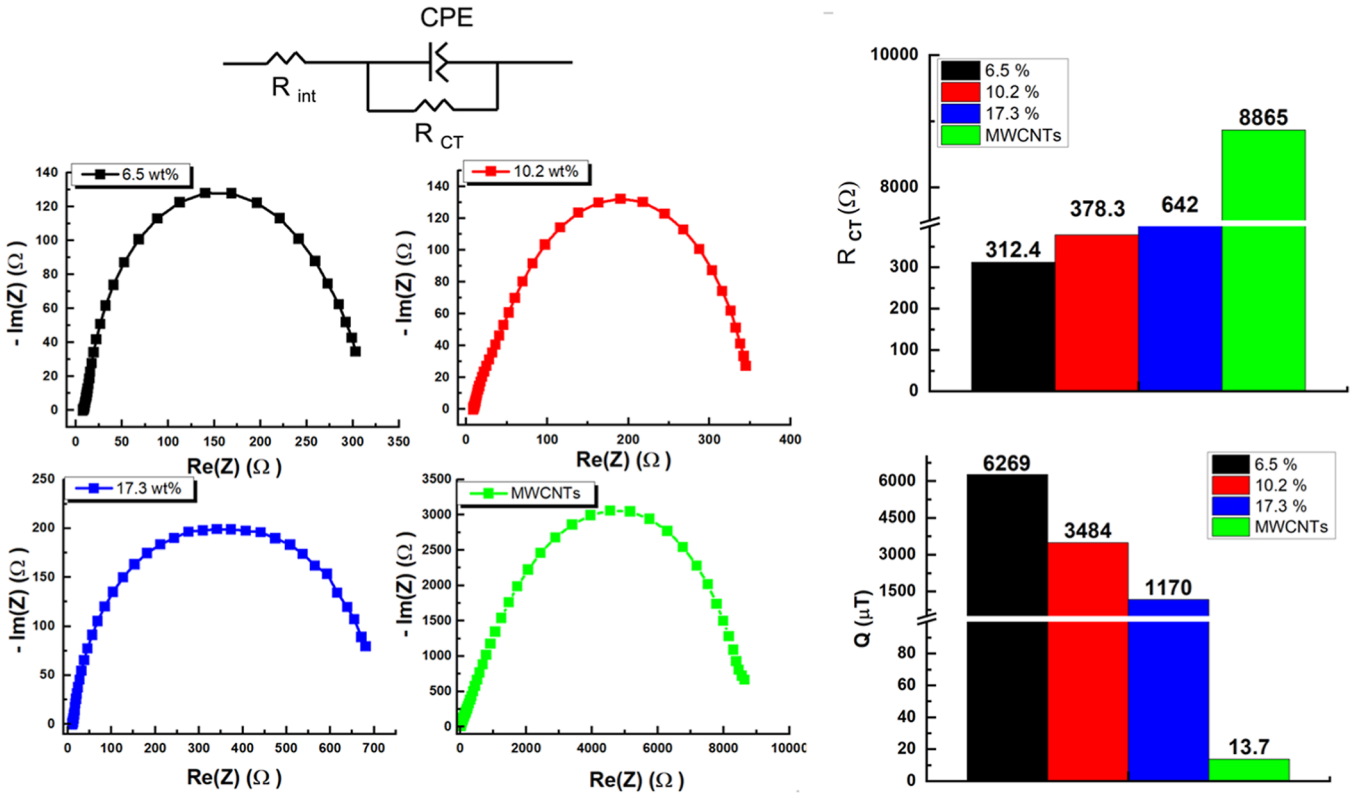

Figure 10. EIS profiles for the different materials (MWCNTs and different loadings of MoS_x@MWCNTs) showing the notable trends of decreasing capacitance and increasing charge-transfer resistance upon increasing the MoS_x wt % in the composite (bar charts).

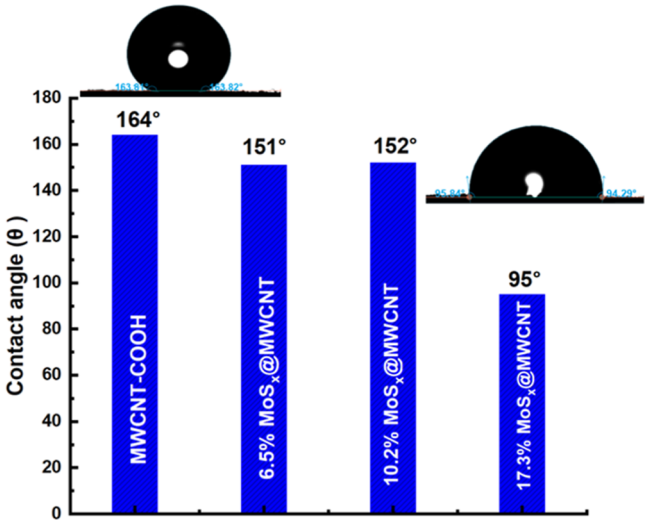

Figure 11. Contact angle measurements made with 0.5 M H_2SO_4 for the MWCNTs used in the synthesis of MoS_x@MWCNTs and the three different composites with increasing MoS_x wt %.

electrolyte used in the electrochemical testing, 0.5 M H_2SO_4 solution. It was observed that the MWCNTs had the most hydrophobic surface, evident by a recorded contact angle of 164°. Upon deposition of MoS_x onto the MWCNTs, the resulted material (MoS_x content of 6.5 and 10.2 wt %) demonstrated reduced hydrophobicity with contact angles of 151 and 152°, respectively. This indicated that the deposition of MoS_x did increase the surface wettability by the electrolyte. Moreover, the sample with 17.3 wt % of MoS_x demonstrated even higher surface wettability with a contact angle of 95°. This experiment pointed to an increased wettability of the catalyst by increasing the MoS_x wt %; however, it also demonstrated that the two catalysts containing 6.5 and 10.2 wt % did have similar wettability, which indicated that differences in their catalytic activities can better be ascribed to factors other than simple surface wettability. Indeed, the most wettable surface is that containing 17.3 wt % of MoS_x, yet it did not show the best performance as a catalyst for the HER, affirming that the surface wettability is not the most significant factor governing the catalyst performance observed herein, but it is rather a combination of surface wettability, charge mobility, and higher abundance of active sites synergistically acting to meditate the optimal performance of the catalyst.

CONCLUSIONS

A gram-scale one-pot solvothermal synthesis is reported for controllable loading of amorphous, mixed-valency MoS_x on MWCNTs. The novel catalyst demonstrated high activity toward the HER with notable low overpotential for the best catalyst containing 6.5 wt % of MoS_x loaded on MWCNTs. The best-performing catalyst demonstrated an overpotential of only 140 mV at 10 mA/cm^2 and 198 mV at 100 mA/cm^2 current density, with a TOF of 0.3 H_2 s^{-1} per Mo atom at η = 200 mV versus RHE. This strategy demonstrated the feasibility for combining the excellent catalytic activity of MoS_x for HER, the enhanced electronic conductivity of the supported catalyst due to the incorporation of the MWCNTs, through a facile synthesis that does not require sophisticated deposition techniques or high-temperature annealing conditions, as well as enabling controllable deposition of the active catalyst on the MWCNTs.

https://doi.org/10.1021/acsanm.2c05311
ACS Appl. Nano Mater. 2023, 6, 3627−3636

■ ASSOCIATED CONTENT

Supporting Information

The Supporting Information is available free of charge at https://pubs.acs.org/doi/10.1021/acsanm.2c05311.

Additional SEM images, additional LSV scans, elemental analysis, and catalyst comparison table (PDF)

■ AUTHOR INFORMATION

Corresponding Authors

Abdou Hassanien − *Jozef Stefan Institute, 1000 Ljubljana, Slovenia;* orcid.org/0000-0002-6774-7518; Email: Abdou.Hassanien@ijs.si

Mohamed H. Alkordi − *Center for Materials Science, Zewail City of Science and Technology, 12578 Giza, Egypt;* orcid.org/0000-0003-1807-748X; Email: malkordi@zewailcity.edu.eg

Authors

Aya Ali − *Center for Materials Science, Zewail City of Science and Technology, 12578 Giza, Egypt*

Mustafa Basuni − *Center for Materials Science, Zewail City of Science and Technology, 12578 Giza, Egypt*

Reham Shams-Eldin − *Center for Materials Science, Zewail City of Science and Technology, 12578 Giza, Egypt*

Lena Pilz − *Institute of Functional Interfaces, Karlsruhe Institute of Technology (KIT), 76344 Eggenstein-Leopoldshafen, Germany;* orcid.org/0000-0002-5616-9003

Tawheed Hashem − *Institute of Functional Interfaces, Karlsruhe Institute of Technology (KIT), 76344 Eggenstein-Leopoldshafen, Germany*

Marita Heinle − *Institute of Functional Interfaces, Karlsruhe Institute of Technology (KIT), 76344 Eggenstein-Leopoldshafen, Germany*

Alexei Nefedov − *Institute of Functional Interfaces, Karlsruhe Institute of Technology (KIT), 76344 Eggenstein-Leopoldshafen, Germany;* orcid.org/0000-0003-2771-6386

Muhamed Amin − *Department of Sciences, University College Groningen, University of Groningen, 9718 BG Groningen, The Netherlands;* Present Address: Laboratory of Computational Biology, National Heart, Lung and Blood Institute, National Institutes of Health, Bethesda, Maryland 20892, USA; orcid.org/0000-0002-3146-150X

Manuel Tsotsalas − *Institute of Functional Interfaces, Karlsruhe Institute of Technology (KIT), 76344 Eggenstein-Leopoldshafen, Germany;* orcid.org/0000-0002-9557-2903

Goran Drazic − *National Institute of Chemistry, 1000 Ljubljana, Slovenia*

Complete contact information is available at: https://pubs.acs.org/10.1021/acsanm.2c05311

Author Contributions

#A.A. and M.B. contributed equally. A.A., M.B., R.S., L.P., T.H., M.H., and A.N. conducted the experiments and results discussion. M.T., M.A., A.H., and M.H.A. interpreted the results, supervised the works, and wrote the manuscript; M.A. conducted the simulations; G.D. conducted STEM imaging; A.H. conducted STM imaging; and M.H.A. conceived the idea, designed the project, wrote the manuscript, and supervised the works.

Notes

The authors declare no competing financial interest.

■ ACKNOWLEDGMENTS

We acknowledge the financial support from the Academy for Scientific Research and Technology (ASRT-Egypt), and the Alexander von Humboldt foundation (Germany). A.H would like to acknowledge the financial support by the Slovenian Research Agency (ARRS) under Program No. P1-0099. We thank Mohamed H. Hassan for helping with the artwork.

■ REFERENCES

(1) Ouyang, L.; He, X.; Sun, Y.; Zhang, L.; Zhao, D.; Sun, S.; Luo, Y.; Zheng, D.; Asiri, A. M.; Liu, Q.; Zhao, J.; Sun, X. RuO2 nanoparticle-decorated TiO2 nanobelt array as a highly efficient electrocatalyst for the hydrogen evolution reaction at all pH values. *Inorg. Chem. Front.* **2022**, *9*, 6602−6607.

(2) Fang, X.; Wang, X.; Ouyang, L.; Zhang, L.; Sun, S.; Liang, Y.; Luo, Y.; Zheng, D.; Kang, T.; Liu, Q.; Huo, F.; Sun, X. Amorphous Co-Mo-B Film: A High-Active Electrocatalyst for Hydrogen Generation in Alkaline Seawater. *Molecules* **2022**, *27*, 7617.

(3) Liu, Q.; Sun, S.; Zhang, L.; Luo, Y.; Yang, Q.; Dong, K.; Fang, X.; Zheng, D.; Alshehri, A. A.; Sun, X. N, O-doped carbon foam as metal-free electrocatalyst for efficient hydrogen production from seawater. *Nano Res.* **2022**, *15*, 8922−8927.

(4) Song, L.; Zhang, X.; Zhu, S.; Xu, Y.; Wang, Y. Hydrogen spillover effect enhanced by carbon quantum dots activated MoS2. *Carbon* **2022**, *199*, 63−69.

(5) Hinnemann, B.; Moses, P. G.; Bonde, J.; Jørgensen, K. P.; Nielsen, J. H.; Horch, S.; Chorkendorff, I.; Nørskov, J. K. Biomimetic Hydrogen Evolution: MoS2 Nanoparticles as Catalyst for Hydrogen Evolution. *J. Am. Chem. Soc.* **2005**, *127*, 5308−5309.

(6) Merki, D.; Hu, X. Recent developments of molybdenum and tungsten sulfides as hydrogen evolution catalysts. *Energy Environ. Sci.* **2011**, *4*, 3878−3888.

(7) Qu, J.; Li, Y.; Li, F.; Li, T.; Wang, X.; Yin, Y.; Ma, L.; Schmidt, O. G.; Zhu, F. Direct Thermal Enhancement of Hydrogen Evolution Reaction of On-Chip Monolayer MoS2. *ACS Nano* **2022**, *16*, 2921−2927.

(8) Zhao, X.; Li, Y.; Zhao, C.; Liu, Z.-H. Hierarchical Ultrathin Mo/MoS2(1−x−y)Px Nanosheets Assembled on P, N Co-Doped Carbon Nanotubes for Hydrogen Evolution in Both Acidic and Alkaline Electrolytes. *Small* **2020**, *16*, 2004973.

(9) Li, G.; Zhang, D.; Qiao, Q.; Yu, Y.; Peterson, D.; Zafar, A.; Kumar, R.; Curtarolo, S.; Hunte, F.; Shannon, S.; Zhu, Y.; Yang, W.; Cao, L. All The Catalytic Active Sites of MoS2 for Hydrogen Evolution. *J. Am. Chem. Soc.* **2016**, *138*, 16632−16638.

(10) Jaramillo, T. F.; Jørgensen, K. P.; Bonde, J.; Nielsen, J. H.; Horch, S.; Chorkendorff, I. Identification of Active Edge Sites for Electrochemical H_2 Evolution from MoS_2 Nanocatalysts. *Science* **2007**, *317*, 100−102.

(11) Benavente, E.; Santa Ana, M. A.; Mendizábal, F.; González, G. Intercalation chemistry of molybdenum disulfide. *Coord. Chem. Rev.* **2002**, *224*, 87−109.

(12) Merki, D.; Vrubel, H.; Rovelli, L.; Fierro, S.; Hu, X. Fe, Co, and Ni ions promote the catalytic activity of amorphous molybdenum sulfide films for hydrogen evolution. *Chem. Sci.* **2012**, *3*, 2515−2525.

(13) Xie, J.; Zhang, J.; Li, S.; Grote, F.; Zhang, X.; Zhang, H.; Wang, R.; Lei, Y.; Pan, B.; Xie, Y. Controllable Disorder Engineering in Oxygen-Incorporated MoS2 Ultrathin Nanosheets for Efficient Hydrogen Evolution. *J. Am. Chem. Soc.* **2013**, *135*, 17881−17888.

(14) Kibsgaard, J.; Chen, Z.; Reinecke, B. N.; Jaramillo, T. F. Engineering the surface structure of MoS2 to preferentially expose active edge sites for electrocatalysis. *Nat. Mater.* **2012**, *11*, 963−969.

(15) Li, H.; Tsai, C.; Koh, A. L.; Cai, L.; Contryman, A. W.; Fragapane, A. H.; Zhao, J.; Han, H. S.; Manoharan, H. C.; Abild-Pedersen, F.; Nørskov, J. K.; Zheng, X. Activating and optimizing MoS2 basal planes for hydrogen evolution through the formation of strained sulphur vacancies. *Nat. Mater.* **2016**, *15*, 48−53.
(16) Lin, S.-H.; Kuo, J.-L. Activating and tuning basal planes of MoO2, MoS2, and MoSe2 for hydrogen evolution reaction. *Phys. Chem. Chem. Phys.* **2015**, *17*, 29305−29310.
(17) Lu, A.-Y.; Yang, X.; Tseng, C.-C.; Min, S.; Lin, S.-H.; Hsu, C.-L.; Li, H.; Idriss, H.; Kuo, J.-L.; Huang, K.-W.; Li, L.-J. High-Sulfur-Vacancy Amorphous Molybdenum Sulfide as a High Current Electrocatalyst in Hydrogen Evolution. *Small* **2016**, *12*, 5530−5537.
(18) Ouyang, Y.; Ling, C.; Chen, Q.; Wang, Z.; Shi, L.; Wang, J. Activating Inert Basal Planes of MoS2 for Hydrogen Evolution Reaction through the Formation of Different Intrinsic Defects. *Chem. Mater.* **2016**, *28*, 4390−4396.
(19) Zhu, J.; Wang, Z.-C.; Dai, H.; Wang, Q.; Yang, R.; Yu, H.; Liao, M.; Zhang, J.; Chen, W.; Wei, Z.; Li, N.; Du, L.; Shi, D.; Wang, W.; Zhang, L.; Jiang, Y.; Zhang, G. Boundary activated hydrogen evolution reaction on monolayer MoS2. *Nat. Commun.* **2019**, *10*, 1348.
(20) Stellmach, D.; Xi, F.; Bloeck, U.; Bogdanoff, P.; Fiechter, S. Catalytic Behavior of Molybdenum Sulfide for the Hydrogen Evolution Reaction as a Function of Crystallinity and Particle Size Using Carbon Multiwall Nanotubes as Substrates. *Z. Phys. Chem.* **2020**, *234*, 1021−1043.
(21) Mei, Y.; Li, T.-T.; Qian, J.; Li, H.; Wu, M.; Zheng, Y.-Q. Construction of a C@MoS2@C sandwiched heterostructure for accelerating the pH-universal hydrogen evolution reaction. *Chem. Commun.* **2020**, *56*, 13393−13396.
(22) Huang, H.; Huang, W.; Yang, Z.; Huang, J.; Lin, J.; Liu, W.; Liu, Y. Strongly coupled MoS2 nanoflake−carbon nanotube nanocomposite as an excellent electrocatalyst for hydrogen evolution reaction. *J. Mater. Chem. A* **2017**, *5*, 1558−1566.
(23) Cao, J.; Zhou, J.; Zhang, Y.; Liu, X. A Clean and Facile Synthesis Strategy of MoS2 Nanosheets Grown on Multi-Wall CNTs for Enhanced Hydrogen Evolution Reaction Performance. *Sci. Rep.* **2017**, *7*, 8825.
(24) Benck, J. D.; Chen, Z.; Kuritzky, L. Y.; Forman, A. J.; Jaramillo, T. F. Amorphous Molybdenum Sulfide Catalysts for Electrochemical Hydrogen Production: Insights into the Origin of their Catalytic Activity. *ACS Catal.* **2012**, *2*, 1916−1923.
(25) Wu, L.; Longo, A.; Dzade, N. Y.; Sharma, A.; Hendrix, M. M. R. M.; Bol, A. A.; Leeuw, N. H.; Hensen, E. J. M.; Hofmann, J. P. The Origin of High Activity of Amorphous MoS2 in the Hydrogen Evolution Reaction. *ChemSusChem* **2019**, *12*, 4383−4389.
(26) Seo, B.; Jung, G. Y.; Lee, S. J.; Baek, D. S.; Sa, Y. J.; Ban, H. W.; Son, J. S.; Park, K.; Kwak, S. K.; Joo, S. H. Monomeric MoS42−-Derived Polymeric Chains with Active Molecular Units for Efficient Hydrogen Evolution Reaction. *ACS Catal.* **2020**, *10*, 652−662.
(27) Laursen, A. B.; Kegnæs, S.; Dahl, S.; Chorkendorff, I. Molybdenum sulfides—efficient and viable materials for electro - and photoelectrocatalytic hydrogen evolution. *Energy Environ. Sci.* **2012**, *5*, 5577−5591.
(28) Tributsch, H. *Ber. Bunsenges. Phys. Chem.* **1977**, *81*, 361−369.
(29) Benck, J. D.; Hellstern, T. R.; Kibsgaard, J.; Chakthranont, P.; Jaramillo, T. F. Catalyzing the Hydrogen Evolution Reaction (HER) with Molybdenum Sulfide Nanomaterials. *ACS Catal.* **2014**, *4*, 3957−3971.
(30) Okpalugo, T. I. T.; Papakonstantinou, P.; Murphy, H.; McLaughlin, J.; Brown, N. M. D. High resolution XPS characterization of chemical functionalised MWCNTs and SWCNTs. *Carbon* **2005**, *43*, 153−161.
(31) Fominski, V.; Demin, M.; Nevolin, V.; Fominski, D.; Romanov, R.; Gritskevich, M.; Smirnov, N. Reactive Pulsed Laser Deposition of Clustered-Type MoSx (x ∼ 2, 3, and 4) Films and Their Solid Lubricant Properties at Low Temperature. *Nanomaterials* **2020**, *10*, 653.
(32) Benoist, L.; Gonbeau, D.; Pfister-Guillouzo, G.; Schmidt, E.; Meunier, G.; Levasseur, A. X-ray photoelectron spectroscopy characterization of amorphous molybdenum oxysulfide thin films. *Thin Solid Films* **1995**, *258*, 110−114.
(33) Ting, L. R. L.; Deng, Y.; Ma, L.; Zhang, Y.-J.; Peterson, A. A.; Yeo, B. S. Catalytic Activities of Sulfur Atoms in Amorphous Molybdenum Sulfide for the Electrochemical Hydrogen Evolution Reaction. *ACS Catal.* **2016**, *6*, 861−867.
(34) Deng, Y.; Ting, L. R. L.; Neo, P. H. L.; Zhang, Y.-J.; Peterson, A. A.; Yeo, B. S. Operando Raman Spectroscopy of Amorphous Molybdenum Sulfide (MoSx) during the Electrochemical Hydrogen Evolution Reaction: Identification of Sulfur Atoms as Catalytically Active Sites for H+ Reduction. *ACS Catal.* **2016**, *6*, 7790−7798.
(35) Dinda, D.; Ahmed, M. E.; Mandal, S.; Mondal, B.; Saha, S. K. Amorphous molybdenum sulfide quantum dots: an efficient hydrogen evolution electrocatalyst in neutral medium. *J. Mater. Chem. A* **2016**, *4*, 15486−15493.
(36) Kibsgaard, J.; Jaramillo, T. F.; Besenbacher, F. Building an appropriate active-site motif into a hydrogen-evolution catalyst with thiomolybdate [Mo3S13]2− clusters. *Nat. Chem.* **2014**, *6*, 248−253.
(37) Huang, Z.; Luo, W.; Ma, L.; Yu, M.; Ren, X.; He, M.; Polen, S.; Click, K.; Garrett, B.; Lu, J.; Amine, K.; Hadad, C.; Chen, W.; Asthagiri, A.; Wu, Y. Dimeric [Mo2S12]2− Cluster: A Molecular Analogue of MoS2 Edges for Superior Hydrogen-Evolution Electrocatalysis. *Angew. Chem., Int. Ed.* **2015**, *54*, 15181−15185.
(38) Vrubel, H.; Merki, D.; Hu, X. Hydrogen evolution catalyzed by MoS3 and MoS2 particles. *Energy Environ. Sci.* **2012**, *5*, 6136−6144.
(39) Chen, Z.; Cummins, D.; Reinecke, B. N.; Clark, E.; Sunkara, M. K.; Jaramillo, T. F. Core−shell MoO3−MoS2 Nanowires for Hydrogen Evolution: A Functional Design for Electrocatalytic Materials. *Nano Lett.* **2011**, *11*, 4168−4175.
(40) Hellstern, T. R.; Kibsgaard, J.; Tsai, C.; Palm, D. W.; King, L. A.; Abild-Pedersen, F.; Jaramillo, T. F. Investigating Catalyst−Support Interactions To Improve the Hydrogen Evolution Reaction Activity of Thiomolybdate [Mo3S13]2− Nanoclusters. *ACS Catal.* **2017**, *7*, 7126−7130.

https://doi.org/10.1021/acsanm.2c05311
ACS Appl. Nano Mater. 2023, 6, 3627−3636